ADVANCED ENERGY MATERIALS
www.advenergymat.de

Visualization of Dissolution-Precipitation Processes in Lithium–Sulfur Batteries

Matthew Sadd, Salvatore De Angelis, Sofie Colding-Jørgensen, Didier Blanchard, Rune E. Johnsen, Simone Sanna, Elena Borisova, Aleksandar Matic, and Jacob R. Bowen**

In this work, light is shed on the dissolution and precipitation processes S8 and Li_2S, and their role in the utilization of active material in Li—S batteries. Combining operando X-ray Tomographic Microscopy and optical image analysis, in real-time; sulfur conversion/dissolution in the cathode, the diffusion of polysulfides in the bulk electrolyte, and the redeposition of the product of the electrochemical reaction, Li_2S, on the cathode are followed. Using a custom-designed capillary cell, positioning the entire cathode volume within the field of view, the conversion of elemental sulfur to soluble polysulfides during discharge is quantitatively followed. The results show the full utilization of elemental sulfur in the cathode in the initial stage of discharge, with all solid sulfur converted to soluble polysulfide species. Optical image analysis shows a rapid diffusion of polysulfides as they migrate from the cathode to the bulk electrolyte at the start of discharge and back to the cathode in the later stages of discharge, with the formation and precipitation of Li_2S. The results point to the redeposition of Li_2S on all available surfaces in the cathode forming a continuous insulating layer, leaving polysulfide species remaining in the electrolyte, and this is the process limiting the cell's specific capacity.

1. Introduction

Lithium-Sulfur (Li—S) cells have attracted much attention over the past decade,[1] thanks to the high theoretical specific capacity (1672 mAh g^{-1}) of sulfur as cathodic material, far exceeding that of state-of-the-art cathodic materials in Li-ion cells. Furthermore, in contrast to materials in standard intercalation-based electrodes,[2] sulfur is highly abundant,[3] has a low cost, and is non-toxic.[3,4] Considering also that a typical sulfur composite cathode contains only sulfur, carbon, and binder, these metrics bear the promise of a sustainable, cost-effective, and high energy density next-generation energy storage technology.

The high specific capacity stems from the conversion reaction where elemental sulfur (S_8) is converted to lithium sulfide (Li_2S) during discharge. The conversion mechanism is complex and multiple reaction pathways have been proposed.[5,6] Common to the different pathways is that it takes place through a series of soluble intermediate polysulfide species (Li_2S_n), where the specific speciation can vary with, for example, electrolyte composition and amount, or operating conditions. Irrespective of pathway, the conversion process leads to several challenges in the realization of practical high energy density Li—S cells.[4,6–8] Polysulfides created during the electrochemical conversion are highly soluble in common liquid electrolytes and their presence in the liquid phase leads to their

M. Sadd, A. Matic
Chalmers University of Technology
Department of Physics
Göteborg 41296, Sweden
E-mail: matic@chalmers.se

S. De Angelis
Paul Scherrer Institute
Electrochemistry Laboratory
Villigen PSI 5232, Switzerland

S. Colding-Jørgensen
Center for Visualizing Catalytic Processes (VISION)
Department of Physics
Technical University of Denmark
Kgs Lyngby 2800, Denmark

The ORCID identification number(s) for the author(s) of this article can be found under https://doi.org/10.1002/aenm.202103126.

DOI: 10.1002/aenm.202103126

D. Blanchard, R. E. Johnsen, S. Sanna, J. R. Bowen
Technical University of Denmark
Department of Energy Conversion and Storage
Roskilde 4000, Denmark
E-mail: jrbowen@xnovotech.com

S. Sanna
Department of Civil Engineering and Computer Science
University of Rome Tor Vergata
Via del Politecnico 1, Roma I – 00133, Italy

E. Borisova
Paul Scherrer Institute
Swiss Light Source
Villigen PSI 5232, Switzerland

J. R. Bowen
Xnovo Technology ApS
Theilgaards Alle 9,1th
Køge 4600, Denmark

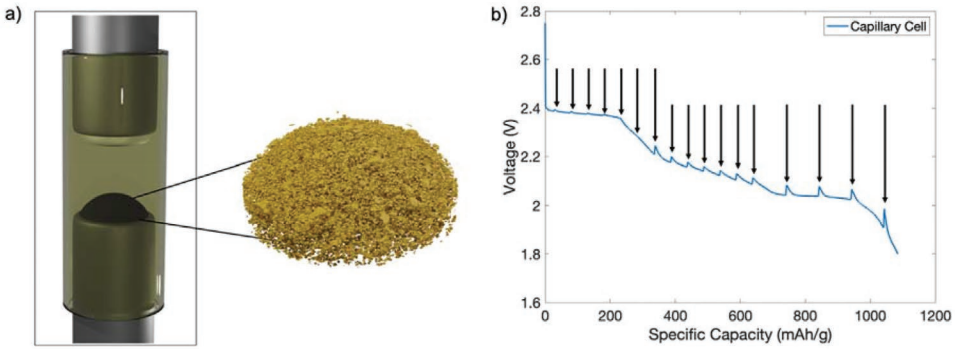

Figure 1. a) Schematic of the capillary cell used for operando measurements with the cathode on the bottom and Li-metal anode on top of the cell. b) Discharge curve of the capillary cell cycled at C/10 during operando tomography. Arrows indicate where tomograms were taken.

diffusion from the cathode to the bulk electrolyte. Due to this diffusion of polysulfides, attention must be paid to the carbon-sulfur cathode microstructure and the effects this will have on cell performance.[9,10] Moreover, the end-product Li_2S has a low solubility in commonly used liquid electrolytes[11,12] and, as soon as it is formed, it precipitates as insulating Li_2S on the cathode surface. Generally, these phenomena lead to a poor utilization of the active material, limiting the specific capacity of Li−S cells. As a result, even though there are several examples in literature showing Li−S cell concepts with an energy density exceeding state-of-the-art Li-ion cells,[13,14] the full capacity is not exploited. Despite some impressive examples of high-performance cells,[15] typically, in high energy density Li−S cells (cells with high active material loading) the specific capacity is only 60–70% of the theoretical value.[16]

A key to reaching the full potential of the technology is to understand the complex processes occurring during discharge of a Li−S cell.[6] Several experimental techniques, including Raman Spectroscopy,[17–20] UV–vis Spectroscopy,[21–23] X-ray Absorption Spectroscopy[24] have been able to determine the speciation of polysulfide species, and digital image analysis[25] has been used to investigate color changes across the electrolyte volume. X-ray Diffraction,[18,26–28] X-ray Photoelectron Spectroscopy, Transmission Electron Microscopy,[9,15] X-ray Transmission Microscopy,[28,29] and X-ray Tomographic Microscopy (XTM)[30–37] on the other hand, can provide information on morphological changes inside the cathode, identifying the formation of insoluble solid S_8 and Li_2S, and associated volume changes of the electrode structure. Many of these techniques are applied as in situ or operando experiments which are crucial considering the complex nature of Li−S chemistry, the conversion reactions, and complex processes of mass transport at play.

In this work, we report on a combination of operando XTM and optical imaging using a custom-built capillary cell, **Figure 1**. This approach allows us to follow the conversion/dissolution and precipitation processes in the cathode as well as diffusion of polysulfides from the cathode and into the bulk electrolyte. With operando XTM we can quantitatively evaluate morphological changes, such as phase fraction and particle size distribution of the active material, in the cathode at different depths of discharge. Previous XTM experiments on Li−S cells have investigated the evolution of Li-metal microstructures[36] as well as the solid phases in the S/C composite cathode during cycling.[30,37] In those experiments the operando cells restricted the field-of-view to less than the full cathode, that is, to local tomography. In contrast, we use a micro-tomography cell geometry,[38] Figure 1 and Figure S1, Supporting Information, chosen to mimic a standard cell configuration while allowing access to full field of view tomography while achieving a small pixel size of 0.325 µm and thus achieving a micrometer spatial resolution. This enables us to quantitatively follow reactions in the Li−S cell and obtain accurate information on phase and morphology changes during cycling and directly correlate this to electrochemical data recorded simultaneously. This is of importance to conclude on the source of active material underutilization and reaction mechanisms. Furthermore, the cell is transparent allowing optical image analysis, simultaneous with the XTM, to provide insights into the mass transport and diffusion kinetics in the liquid electrolyte phase of the bulk polysulfide speciation, with greyscale intensity showing an increase in polysulfide concentration in the electrolyte. The results from the operando XTM experiment are corroborated by ex situ analysis of cathodes retrieved from cycled coin cells.

With the combination of operando XTM and image analysis, used to quantify changes in the cathode and the electrolyte, we demonstrate that the underutilization of active material is connected to the last stage of the sulfur conversion process, the formation of Li_2S, and show that the diffusion of polysulfides in and out of the electrolyte and Li-ions into the cathode are crucial processes for efficient polysulfide conversion and control the reaction kinetics in the cell.

2. Results and Discussion

2.1. Operando Tomography

2.1.1. Sulfur Dissolution

With the operando tomography experiment, we follow in real-time the evolution of the capillary cell cathode morphology, directly visualizing sulfur conversion/dissolution and redeposition processes. The voltage profile of the capillary cell (Figure 1b) displays the typical behavior of a Li−S cell, including voltage spikes associated with exposure to the x-ray beam.[12] The first voltage plateau, at 2.4 V, extends to 230 mAh g^{-1} of

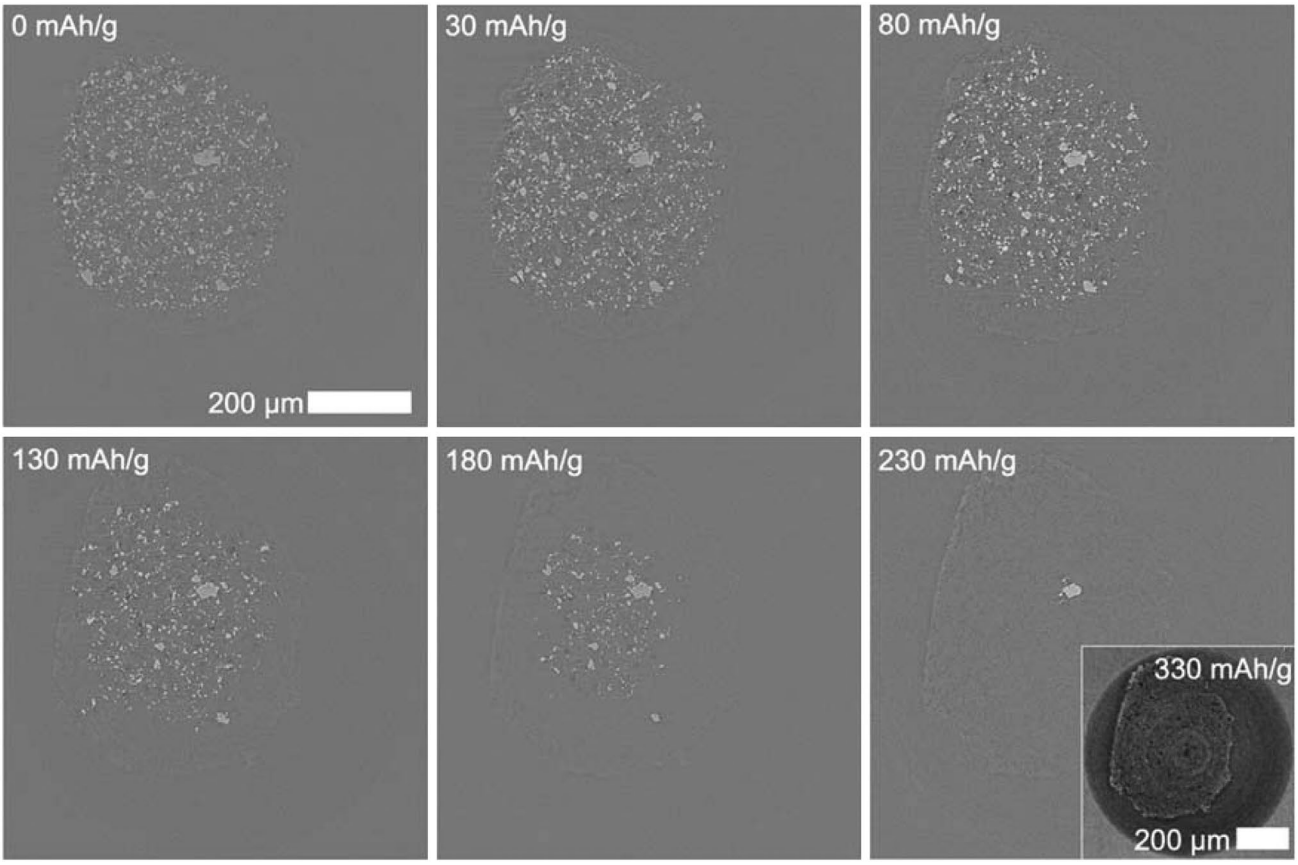

Figure 2. Absorption contrast tomographic slices, parallel to the current collector and extracted from the 3D volume, taken during the initial stages of discharge following the progress of sulfur conversion and dissolution. Sulfur particles appear as the brightest phase in the images (Figure S2, Supporting Information). Inset shows a Paganin reconstructed tomographic slice obtained at the end of the first discharge plateau with enhanced contrast between the carbon matrix and electrolyte. The contrast of the images has been adjusted for the purposes of visualization. High-resolution images are found in Figure S3, Supporting Information.

discharge and is commonly associated with the conversion of elemental sulfur according to:

$$S_8 + 2Li^+ + 2e^- \rightarrow Li_2S_8 \quad (1)$$

Though other conversion pathways have been proposed, with the formation of shorter chain polysulfide species directly from elemental sulfur,[5] for the conditions of this experiment, the capacity from the 2.4 V plateau and the color of the electrolyte[39] agree with the formation of Li_2S_8 as previously proposed.[6,40]

The subsequent region in the discharge curve, presenting a sloping voltage, is typically a result of the interconversion of dissolved polysulfide species, from long polysulfide chains to short chains:

$$Li_2S_8 + 2e^- + 2Li^+ \rightarrow Li_2S_{8-n} + Li_2S_n \ (n = 4-6) \quad (2)$$

The second plateau extends to the end of discharge, with the onset of polarization at 1000 mAh g^{-1}, and is associated with the conversion of short-chain polysulfide species to insoluble Li_2S:

$$Li_2S_n + (2n-2)2e^- + (2n-2)Li^+ \rightarrow Li_2S_{8-n} + nLi_2S \quad (3)$$

The end product (Li_2S) has been stated to have a variety of morphologies depending on the solvent used in liquid electrolytes, from the formation of large crystals, to the formation of a film-like layer.[41] With further work identifying the Li_2S layer as both porous,[42] and depending on the substrate, even amorphous.[15]

In the 2D slices shown in **Figure 2**, sulfur is the brightest phase, carbon appears as light grey, and pores in the carbon structure are dark grey, see also Figure S2, Supporting Information. At increasing depth of discharge, we observe the disappearance of sulfur particles and the appearance of pores in the cathode. In the tomogram taken at 330 mAh g^{-1} (Figure 2), after the first plateau, sulfur particles can no longer be observed, and pores appear from sites that originally hosted sulfur particles (Figure S2, Supporting Information). We also expect to have an intrinsic porosity of the carbon/binder host matrix. However, these pores are below the resolution limit of our experiment.

The data in Figure 2 indicates that between 200 and 300 mAh g^{-1} into discharge all elemental sulfur has been converted into polysulfides and dissolved in the electrolyte. It should be noted that even though the XTM slices do not show the presence of sulfur, there is the possibility of the presence of sulfur particles that reduce in size below the resolution limit of the experiment. To limit this effect the sulfur used to prepare the cathode was sieved to achieve an initial particle size range of 32–45 µm, see methods section. **Figure 3**a–d shows volume renderings of all sulfur particles in the cathode of the operando capillary cell and

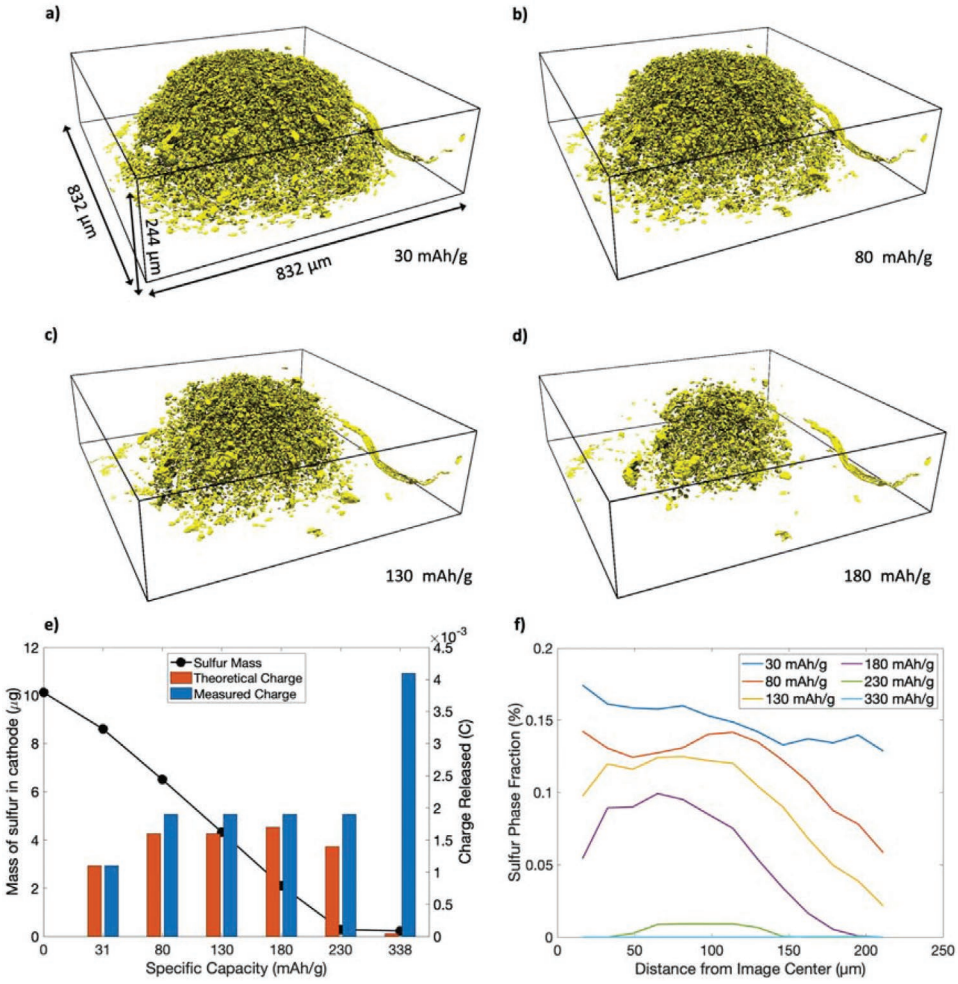

Figure 3. a–d) Volume renderings of cathode sulfur and e) Total sulfur mass in the cathode as a function of the specific capacity, determined from volume renderings of elemental sulfur (black) and theoretical charge released, calculated from the conversion of elemental sulfur in the cathode determined from the volume renderings (orange) to Li_2S_8 and the actual measured charge between tomograms from the cycling experiment (blue). f) Radial distribution of sulfur within the cathode at different depths of discharge.

further demonstrates the dissolution of the elemental sulfur. Since all elemental sulfur is within the field of view, we can quantitatively link the tomographic and electrochemical data. Figure 3e shows the total sulfur mass in the electrode, determined from the volume of segmented S_8 multiplied with the mass density, (see methods section), as a function of the depth of discharge. A linear decrease in the amount of sulfur in the cathode (constant dissolution rate) is observed as expected for galvanostatic discharge. Theoretically, the full conversion of elemental sulfur to Li_2S_8 (Equation (1)) corresponds to a specific capacity of 208 mAh g^{-1}, which agrees with the absence of elemental sulfur in tomograms after 230 mAh g^{-1}, that is, during the first plateau in the discharge curve (Figure 1b). However, the ≈2.4 V plateau extends to 230 mAh g^{-1}, 22 mAh g^{-1} more than would be theoretically expected, which implies that the conversion of Li_2S_8 to shorter chain polysulfides (Equation (2))) also takes place in this region. The presence of the process of further conversion of polysulfides is also reflected in the slightly sloping voltage profile.

Further support of the early start of further conversion to shorter chain polysulfides can be found in Figure 3e which directly compares the theoretical charge originating from the conversion of S_8 to Li_2S_8 (blue), based on the tomography data, to the actual charge released by the cell between each tomogram determined from the electrochemical cycling data (orange). Initially, at 31 mAh g^{-1} into discharge, the observed and theoretical charges are equal, showing that at this stage there is only the conversion of S_8 to soluble polysulfide species (Equation (1)). However, in the following steps, until a capacity of 180 mAh g^{-1} is reached, more charge is released compared to the theoretical prediction related to the conversion of elemental sulfur. Therefore, the extra capacity observed in the first plateau provides direct evidence that the conversion of long-chain polysulfide species to shorter chain polysulfides (Equation (2)) and the conversion of elemental sulfur occurs simultaneously. The contribution from further conversion of polysulfides is evident when one considers the measured capacity at 338 mAh g^{-1} into discharge where virtually no elemental sulfur is present in the cathode.

One could also consider the possibility that the extra capacity in the region of the first plateau may be the result of side reactions, such as electrolyte decomposition. Previous

literature does not suggest such processes in the initial cycles.[43] When observed, electrolyte decomposition is most prevalent during charge,[44] and the commonly known reduction of $LiNO_3$ is only observed below 1.85 V,[45] and is not considered to contribute to capacity in the 2.4 V plateau. Furthermore, all elemental sulfur in the cathode participates in the first step of the discharge process, that is, it is converted to polysulfide and contributes to the cell's capacity. Thus, the limited specific capacity must be sought after in the later steps of the electrochemical conversion process, following the conversion of elemental sulfur.

The 3D renderings of the elemental sulfur in Figure 3a–d qualitatively show that the active material volume shrinks radially, that is, that the conversion/dissolution process of elemental sulfur slows down from the cathode surface towards the core of the electrode. Quantitatively, this is shown in Figure 3f, where the radial sulfur phase fraction from a single 2d cut of the cathode is plotted as a function of discharge in the region of the first plateau in the voltage profile. This analysis shows that as the discharge progresses, sulfur particles far away from the electrode center experience a higher dissolution rate at early stages of discharge, demonstrated by the pronounced drop of the sulfur phase fraction profiles with increasing distance from the center of the electrode. However, the conversion/dissolution clearly occurs throughout the whole cathode, demonstrated by the continuous decrease in the sulfur phase fraction in the center of the cathode with discharge. One can also note that once all elemental sulfur has been converted and dissolved in the outer layer of the cathode (the outer 75–100 μm) we will also have very fast kinetics in the core, as can be seen by the fast decrease in sulfur phase fraction after 130 mAh g^{-1} into discharge (Figure 3f). Although the fastest dissolution rate is seen furthest from the cathode center, there is also a drop in concentration in the image center. This is an artifact of the volume integration where the center volume is so small that the statistical error in finding an active material particle is large.

The conversion/dissolution behavior followed by operando XTM can be rationalized by considering that the electrochemical reaction rate is dependent on the local polysulfide concentration and Li-ion flux to, and in, the electrode. From the surface of the electrode, dissolved polysulfides can diffuse out in the bulk electrolyte, driven by the polysulfide concentration gradient, keeping the local polysulfide concentration relatively low allowing further polysulfide dissolution. Similarly, flux of Li-ions from the bulk electrolyte to the cathode ensures that the conversion reactions can be sustained. In the center of the electrode, the local polysulfide concentration will be higher since their diffusion is limited by a longer, and less effective, diffusion pathway through the carbon-binder matrix, a lower local chemical concentration gradient, and a lower diffusivity due to an increase of the electrolyte viscosity due to the increased local polysulfide concentration. This will slow down polysulfide dissolution in the center of the cathode. Furthermore, the diffusion of Li^+ will also be limited, leading to a depletion of Li-ions which also slows down the conversion rate.

To quantify the sulfur particle dissolution across the cathode volume, Figure S4, Supporting Information, shows the evolution of the sulfur particle size distribution (PSD) as a function of discharge. In the pristine state, the majority of sulfur particles have an equivalent diameter of ≈10 μm, as shown by the peak of the PSD in Figure S4, Supporting Information. The overall shape of the PSD distribution remains unchanged during discharge, with the integrated area of different curves only decreasing due to the decrease of the sulfur volume in the cathode. This result shows that, for the conditions of this experiment, both small and large particles dissolve at approximately the same rate (i.e., no peak shift of the curve), however the particle size distribution is also not that large. Thus, the initial morphology of our S/C composite cathode does not limit the active material utilization, but for thicker cathodes or higher discharge rates, the progressively slower conversion and dissolution processes in the center of the cathode could lead to active material not being exploited unless one ensures efficient diffusion of polysulfides out from the cathode and Li^+ into the cathode. As an estimate, one can consider that the conversion kinetics increases rapidly in the core of the cathode after 30 min into discharge (after 130 mAh g^{-1}). Thus, at discharge rates approaching this time scale one can expect underutilization of active material with elemental sulfur remaining unconverted in the electrode.

2.1.2. Li_2S Deposition

Figure 4 shows tomogram slices through the cathode of the operando cell during the later stages of discharge, that is, when all elemental sulfur has been converted to soluble polysulfide species (>330 mAh g^{-1}). In this range, the conversion to Li_2S, and its subsequent precipitation on the cathode surface, is expected to occur as a result of supersaturation of the electrolyte and nucleation of Li_2S.[46–48] To observe the presence of precipitated Li_2S in the cathode structure, the slices in Figure 4 have been reconstructed using the Paganin method to obtain phase contrast data,[49] enhancing the contrast between the carbon-binder cathode matrix and the precipitated Li_2S. A clear increase in grayscale intensity is observed after 740 mAh g^{-1} (Figure 4h), linked to the deposition of Li_2S, and is quantified in Figure 4l.

From the 2D tomographic slices, it is clear that Li_2S is continuously deposited throughout the 2.1 V plateau and that it is uniformly distributed over the cathode structure. Individual Li_2S particles cannot be resolved which suggests that they are smaller than the resolution (1 μm) in the XTM experiment, in agreement with previous results reported in literature.[42] The deposition of small particles leads to a uniform coverage of the cathode's surfaces and the formation of a continuous Li_2S layer. Since Li_2S is an electrical insulator, this layer cannot act as a surface where electron transfer with remaining polysulfides dissolved in the electrolyte can occur. This Li_2S layer has previously been described as porous,[42] which can limit diffusion of polysulfide species and Li^+, thus hindering their access to the carbon surface for electron transfer, as indicated by the onset of polarization in the discharge curve shown in Figure 1b, limiting the cell's specific capacity.

2.2. Ex Situ Coin Cell Validation

The capillary cell configuration provides a suitable geometry to monitor the morphological changes within the cathode while

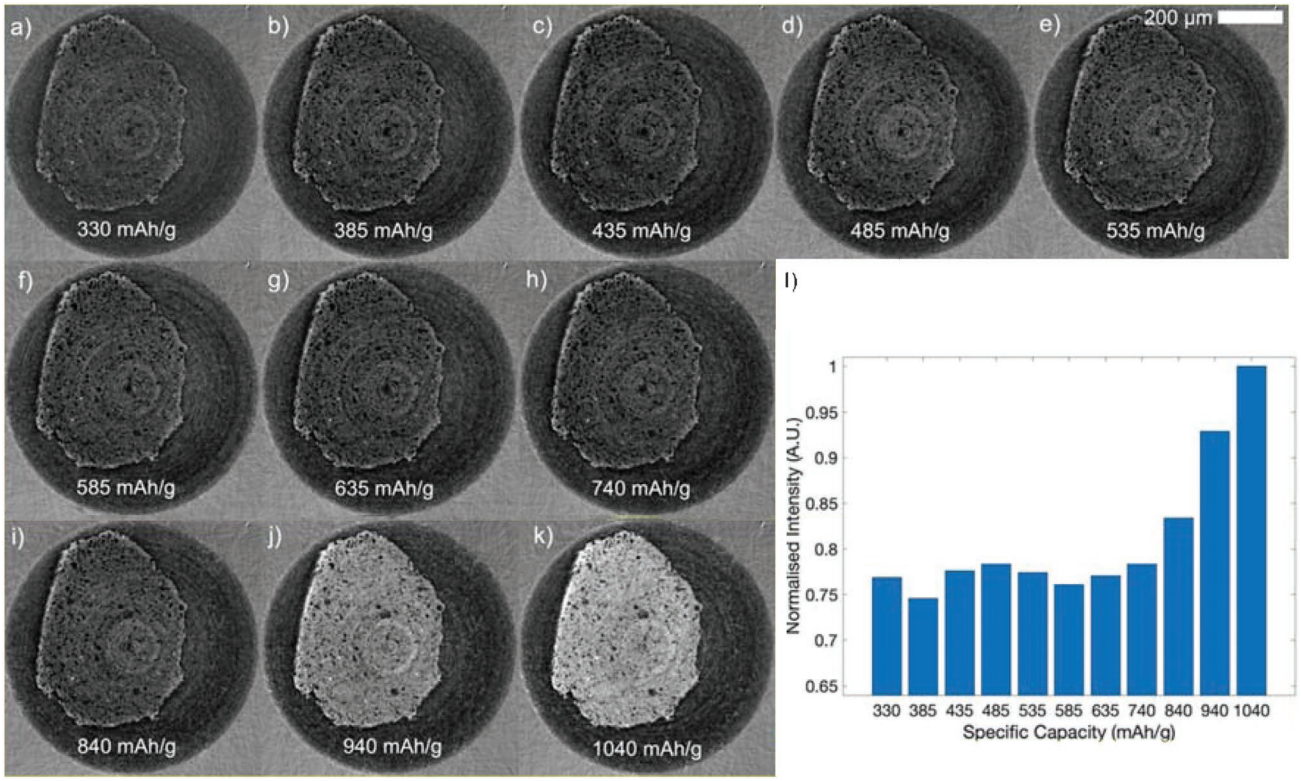

Figure 4. a–k) 2D tomographic slices of the cathode in the operando cell after the initial stage and up to full discharge (330 to 1040 mAh g^{-1}) from the same location as Figure 2. l) Average cathode intensity, normalized to the average intensity at 1040 mAh g^{-1}, as a function of depth of discharge. High-resolution images are provided in Figure S5, Supporting Information.

keeping it in the field of view of the tomography experiment. However, it should be noted that the cell does not contain a separator and that the electrolyte volume is large. Therefore, to benchmark the operando capillary cell data, we performed ex situ XTM experiments on separate cathodes retrieved from coin cells at various depths of discharge. Overall, the results from the operando experiment are congruent with the observations from ex situ analysis. The specific capacities of the two cells are quite similar (1084 and 1112 mAh g^{-1} for the operando and coin cells, respectively, 65% of the theoretical capacity, **Figure 5**a) showing that the capillary cell is a valid model system. Thus, the electrochemical reactions should be the same even though we have flooded conditions in the capillary cell and leaner conditions in the coin cell (10 µL mg^{-1} of sulfur).

Figure 5b/g, shows a cathode in a pristine state, with the current collector seen at the bottom of the image, followed by the sulfur/carbon composite, with sulfur clearly visible. 2D slices from tomograms of cathodes retrieved from cells cycled to 100 and 200 mAh g^{-1} (Figure 5c/h, and Figure 5d/i) respectively both show similar results, with some evidence of sulfur remaining in the cathode and the formation of pores. In agreement with the results from the capillary cell, in the coin cells, all elemental sulfur has been converted to polysulfide species and dissolved by the electrolyte between 200 (Figure 5d/i) and 300 mAh g^{-1} (Figure 5e/j) into discharge. This confirms the finding that there is no underutilization of elemental sulfur and that the limited specific capacity of the cell must be linked to later stages of the electrochemical conversion reaction. Furthermore, also in the coin cell configuration, we find that the start of further conversion of Li_2S_8 to short-chain polysulfides takes place in the region of the first plateau, as evidenced by the 42 mAh g^{-1} extra capacity compared to that theoretically expected for conversion of elemental sulfur. As for the capillary cell, the fully discharged cathode (Figure 5f/k) reveals a homogenous morphology showing that the redeposition of Li_2S occurs uniformly on all available surfaces. The Li_2S particle size is below the resolution of the experiment, following the same pattern as was observed for the cathodes in the capillary cell. To verify that the end-product is Li_2S, Figure S6, Supporting Information, shows an XRD pattern from a cathode retrieved from a coin cell after full discharge. The peak at 2theta = 27° (using Cu K-α) is a signature of the presence of Li_2S.[18] The relatively large width of the peak indicates that the crystallize size is small and/or that there is a structural disorder. In addition, no characteristic signatures for Li_2S_2 are found, see Figure S6, Supporting Information. The overall agreement of the results from the capillary and coin cells validates the relevance of the geometry and setup of the capillary cell, without a separator and a larger electrolyte volume.

2.3. Operando Optical Image Analysis

During polysulfide formation, after the conversion of elemental sulfur at the start of discharge, polysulfides are expected to

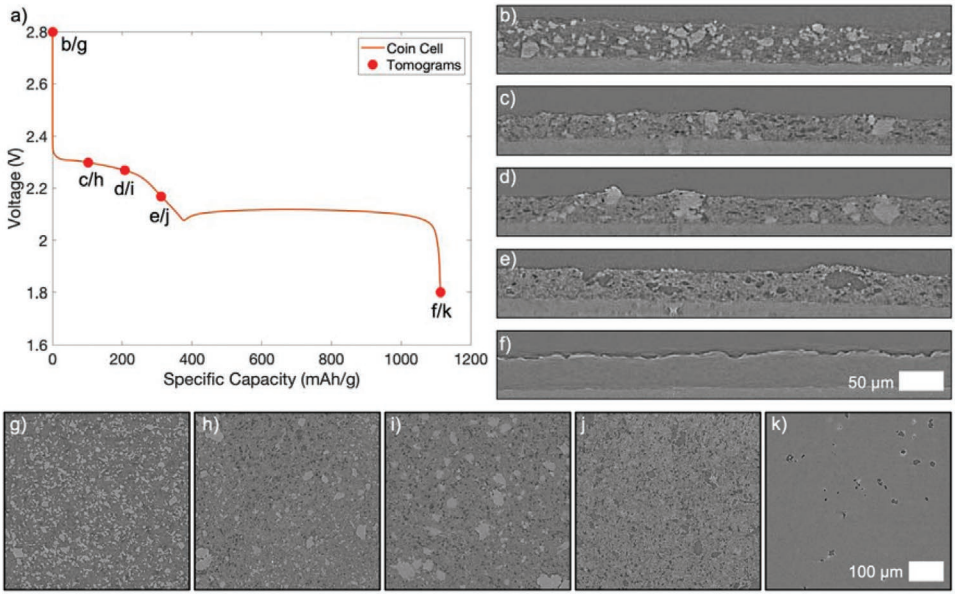

Figure 5. a) Typical discharge voltage profile for Li—S coin cells used for ex situ tomography. b–f) perpendicular and g–k) parallel to the current collector 2D slices from tomograms of pristine, ≈100 mAh g^{-1}, ≈200 mAh g^{-1}, ≈300 mAh g^{-1}, and fully discharged cathodes (1112 mAh g^{-1}), respectively. In the perpendicular slices, the Al-current collector is at the bottom followed by the cathode coating. Individual voltage profiles are shown in Figure S7, Supporting Information.

diffuse out of the cathode into the bulk electrolyte, driven by the developing concentration gradient of the polysulfide species between the cathode and the bulk electrolyte. To quantify the distribution and diffusion of polysulfides in the bulk electrolyte during discharge we performed an operando experiment using the analysis of optical images, where we monitor the greyscale intensity change of the electrolyte color in the capillary cell due to the presence of polysulfides.[22] With this method, individual polysulfide species cannot be distinguished, however, the greyscale intensity derived from the intensity of the electrolyte color across the cell can be quantified, providing information on the changes of polysulfide concentration as a result of diffusion of polysulfide species through the cell. As seen in **Figure 6**a and Figure S8, Supporting Information, as discharge proceeds, the electrolyte darkens. The color change during discharge is quantified by converting the images to greyscale and determining the greyscale intensity. Figure 6b–d shows the result of this analysis, where the presence of polysulfides can be tracked providing information on their distribution in the cell as a function of depth of discharge.

At the start of discharge, around 50 mAh g^{-1}, there is a rapid increase in grayscale intensity, Figure 6b. This correlates well with the dissolution of soluble polysulfides, and the delay of 50 mAh g^{-1} suggests a delay in the diffusion of polysulfide species out of the cathode, enabling the onset of further conversion of the long-chain polysulfide species to short-chain polysulfides. The intensity increase occurs almost simultaneously throughout the cell pointing to a very rapid diffusion of polysulfides driven by the concentration gradient, Figure 6b,c. At 40 mAh g^{-1} into discharge a very shallow minimum is observed in the intensity profile over the cell (Figure 6c). This is most likely caused by a fluctuation in the glass capillary at this specific position resulting in an apparent local intensity decrease. Thus, this change in intensity between the middle of the electrolyte and the anode is not related to a specific physical process and can be considered within the error of the experiment.

The intensity reaches a maximum at around 300 mAh g^{-1}, correlating well with the full conversion of elemental sulfur, as demonstrated by the tomography data, Figure 2. The maximum intensity is almost the same at the cathode and the anode, underlining the even distribution of polysulfides throughout the whole cell. The rapid drop in intensity after the first plateau, around 300 mAh g^{-1} into discharge, can be attributed to the further conversion of polysulfide species to shorter chain species (Li_2S_n, n = 3–6), which causes the electrolyte to turn lighter in color, as previously demonstrated and reported with UV–vis spectroscopy.[22] The rate of the intensity decrease between 300–450 mAh g^{-1} is the same throughout the cell and there is only a very small concentration gradient over the bulk electrolyte at this stage, as a result of the rapid diffusion of polysulfides in the electrolyte. Approaching full discharge, the conversion of short-chain polysulfides to insoluble Li_2S is the dominating process in the cathode, decreasing the overall concentration of polysulfides in the cell. To sustain the electrochemical process, polysulfides must move back from the bulk electrolyte and towards the cathode and, as this process proceeds, a concentration gradient is built up in the bulk electrolyte (Figure 6c). A slow continuous decrease in intensity is observed at the anode and in the middle of the electrolyte, whereas the intensity at the cathode remains constant (Figure 6b) approaching full discharge. Previous UV–vis experiments have shown that different polysulfide species absorb in different parts of the visible spectrum, that is, the electrolyte can change color depending on dissolved polysulfide species.[22,50] However, Figure S8, Supporting Information, shows that throughout the discharge process there is not a very large color change in the electrolyte, especially

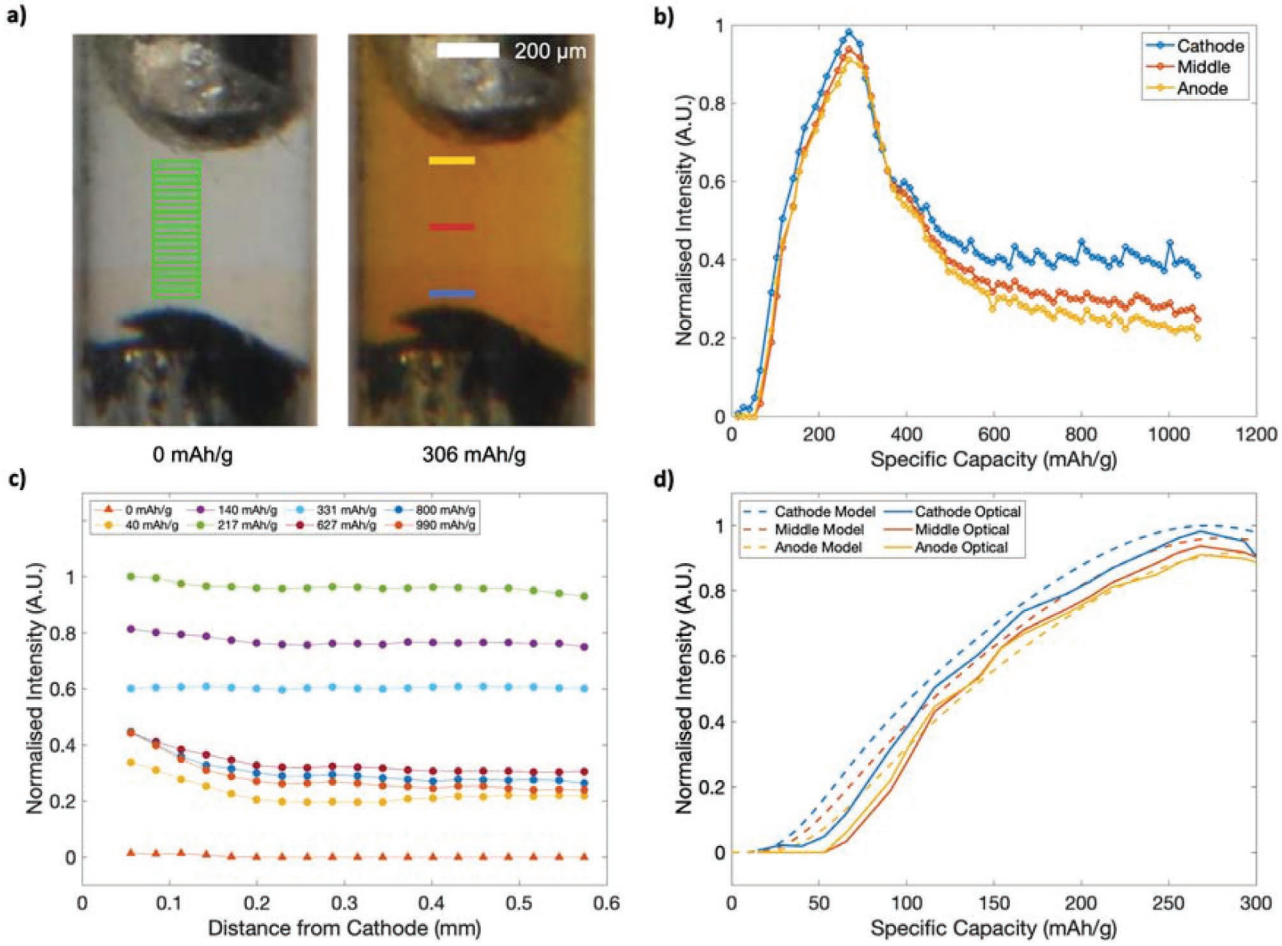

Figure 6. Optical image analysis of operando capillary cell showing polysulfide distribution in the electrolyte. a) Photograph of the cell before discharge and at 306 mAh g^{-1} into discharge. The analyzed regions in Figure b, c, and d are indicated. b) Normalized greyscale intensity as a function of depth of discharge close to the cathode, in the middle of the electrolyte, and close to the anode. c) Normalized greyscale intensity as a function of distance from the cathode at different depths of discharge. d) Normalized greyscale intensity compared to the results from the diffusion model.

in the latter part of discharge the color is the same, in agreement with previously reported experiments.[25] Our results show that the migration of polysulfides from the bulk electrolyte to the cathode, against the concentration gradient, is crucial to sustaining the electrochemical reaction. At full discharge, there is a finite greyscale intensity throughout the bulk electrolyte showing that polysulfide species remain dissolved in the electrolyte. This observation agrees with the electrochemical data where the specific capacity at full discharge was determined to 1040 mAh g^{-1} compared to 1672 mAh g^{-1} expected theoretically for full active material utilization. This suggests that the limiting process during discharge of the Li−S cell is the conversion of dissolved PS species to Li_2S. As this process slows down, due to the decrease in available surface sites for Li_2S deposition, the concentration of polysulfides within the electrolyte remains constant during the final stages of the discharge process when the cell polarizes and reaches the lower voltage cut-off.

To quantify the migration of polysulfides during the initial stage of discharge we apply a 1D model, based on Fick's laws (Equation (1)), to simulate the diffusion of polysulfides in the bulk electrolyte, observed experimentally and shown in Figure 6d.

$$J = -D\frac{dC}{dx} \text{ and } \frac{dC}{dt} = D\frac{d^2C}{dx^2} \quad (4)$$

The model takes into account the flux of PS species, J, concentration gradient, C, and the diffusion coefficient, D. A detailed description of the model and parameters can be found in the Supporting Information. The source of polysulfides in the simulations was obtained from the S_8 dissolution rate determined from the tomography data (Figure 3e and Figure S9, Supporting Information). The simulation domain was divided into two subdomains, the cathode, and the bulk electrolyte, with different diffusion coefficients for polysulfides, $D_c = 9.5\ 10^{-8}$ cm^2 s^{-1} and $D_e = 7.5\ 10^{-6}$ cm^2 s^{-1}, respectively, obtained from the fit of the simulation to the experimental data. D_c represents the diffusion in the 3D percolating network of the cathode and the lower value, compared to the bulk electrolyte, is a result of both the geometrical constraints, that is, higher tortuosity of the diffusion pathways and of the increased electrolyte viscosity due to

the higher local concentration of polysulfides. D_e represents the free diffusion in the bulk electrolyte and agrees with published values.[51] This simple model reproduces, with good agreement, the evolution of the polysulfide concentration in the bulk electrolyte (Figure 6d). The maximum concentration is obtained at the same depth of discharge as the maximum in greyscale intensity in the experimental data and the increase in concentration exhibits a similar rate. The difference in concentration between the three locations (anode, middle, and cathode) is more pronounced compared to the experimental data, especially at the start of the discharge. The observed deviations could be explained by the 1D of the model, which does not consider the diffusion towards the cathode current collector which may arise before the electrolyte becomes locally saturated. Though there are other potential mass transport processes that could potentially contribute to the motion of polysulfides through the lithium-sulfur cell, for example, convection or electromigration, our simulation results show that during the first discharge plateau and for the discharge rate used in this study (C/10), the polysulfide mass transport is diffusive and appears to be mainly governed by the concentration gradient of polysulfide species. This diffusion is rapid enough to equalize the concentration in the bulk electrolyte and thus limit the build-up of large concentrations of polysulfide species close to the cathode which would limit the conversion of S_8 to polysulfide species.

3. Conclusions

From our combined operando XTM and optical analysis, we demonstrate that with a full field of view tomography we can quantitatively follow the initial conversion of elemental sulfur with the subsequent dissolution of the formed polysulfides species, as well as the diffusion of polysulfides to the bulk electrolyte during the initial stage of discharge. Furthermore, we were able to track the migration of polysulfides back to the cathode followed by the precipitation of Li_2S on the carbon-binder matrix at the end of discharge. Our results show that all elemental sulfur in the cathode is converted, and the conversion products are fully dissolved by the electrolyte. The conversion kinetics slow down radially towards the center of the electrode. We attribute this to the increased local concentration of PS species, due to slower diffusion within the porous electrode and an increase of the local electrolyte viscosity, as well as a decrease in the flux of Li^+ slowing down the conversion reaction.

By comparing the theoretical charge that can be obtained from the conversion of elemental sulfur to the actual charge measured experimentally, we also find that the interconversion of polysulfides starts almost immediately. As soon as there is Li_2S_8 available, it is further converted to form shorter chain species. From the optical analysis, we find that the polysulfides formed in the cathode rapidly diffuse out of the cathode structure into the bulk electrolyte. This process starts immediately at the beginning of the discharge process, and is rapid, as such almost no intensity gradient can be observed in the cell. To sustain the electrochemical process with further interconversion of polysulfides when all elemental sulfur is converted, we observe a migration of polysulfides back to the cathode.

From our data, we find a uniform deposition of Li_2S, with a particle size smaller than the tomographic resolution (< 1 µm), on the cathode. At this resolution it is observed that the precipitates cover the entire surface of the cathode, effectively blocking further conversion of polysulfides still present in the electrolyte. One should note that the morphology of Li_2S deposits will depend on the electrolyte formulation and could be resolved in an operando XTM experiment using electrolytes where larger crystallites are formed.

From our results, it is evident that the initial morphology of our S/C composite cathode is not of significant importance when it comes to the utilization of active material, in the sense that the final precipitation takes place everywhere in the cathode and not only in the pores formed initially as elemental sulfur particles dissolve. However, from the fact that the conversion and dissolution processes slow down towards the center of the cathode, one can infer that for thicker cathodes, or high discharge rates, elemental sulfur could remain unconverted in case the morphology does not allow rapid diffusion of polysulfides out from the cathode and/or Li^+ into the cathode.

From the comparison of our operando data to ex situ samples from coin cells, we can conclude that the capillary cell is a good model system, despite the difference in geometry and electrolyte volume. The full field of view, enabled by the use of the capillary cell, is crucial to extract quantitative information that can be directly correlated with electrochemical data recorded simultaneously. Thus, full-field tomography is an important path forward for correlative experiments to link dissolution/precipitation processes in Li−S cells to their electrochemical response, the determination of rate-limiting processes, and the role of the cathode microstructure.

Further investigations using XTM, and optical analysis of the electrolyte, would benefit from variations to the cathode structure and sulfur content to investigate the diffusion of species through pores. Such experiments should vary the cathode thickness, and hierarchical structures, for instance, the use of carbon nanofibers. Furthermore, to gain greater insights into the effect of the diffusion of polysulfide throughout the electrolyte, future experiments would benefit from using higher current densities, to increase the rate of conversion in the cell, as well as systematically investigating the influence of electrolyte volume when moving to lean conditions, with electrolyte to sulfur ratios for instance below 6 µL mg^{-1}.

4. Experimental Section

Cathode Formulation: The cathode slurry was a mix of 60% wt. sulfur, 30% wt. Super P carbon black (Alfa Aesar), and 10% wt. PVDF (Arkema) in N-Methyl-2-Pyrrolidone (Sigma Aldrich, 99.5% anhydrous). To ensure that the majority of sulfur particles were detectable given the XTM resolution, sulfur powder (Sigma Aldrich, 99%) was sieved using an ethanol suspension, collecting particles between consecutive sieves having 45 and 32 µm mesh opening.

Coin Cell Fabrication: The cathode slurry was coated onto aluminum foil using a doctor blade at a thickness of 250 µm. Coin cells were assembled using cathodes coated onto Al foil (sulfur loading 1 mg cm^{-2}), a Celgard 2400 separator, and a lithium metal foil. 15 µL of 1 M LiTFSI (Solvionic, 99.9%, extra dry) and 0.25 M $LiNO_3$ (Sigma Aldrich, 99.99%) in 1,2-dimethoxyethane (Sigma Aldrich, anhydrous,

99.5%) and 1,3-dioxolane (Sigma Aldrich, anhydrous 99.5%) in a 1:1 volume ratio was used as the electrolyte.

Capillary Cell Fabrication: The capillary cell (Figure 1 and Figure S1, Supporting Information) was developed from the design described by Johnsen and Norby.[38] A 316 stainless steel current collector, diameter 700 µm and length of 3 cm, was dip-coated with the cathode slurry described above and dried at 70 °C for at least 60 min, to evaporate the solvent. The procedure was performed twice to obtain the final electrode (sulfur loading 2.5 mg cm^{-2}). The coated current collector was inserted in a glass capillary, inner diameter 700 µm, and fixed by Cyberbond U3600 UV-curable adhesive. The capillary was filled with the same liquid electrolyte as used in the coin cells described above. A second steel rod coated with metallic lithium was used as anode. The assembly of the capillary cell, electrolyte filling, and insertion of the anode, was performed in a glovebox with controlled Ar atmosphere (O_2 and H_2O level < 1 ppm).

Electrochemical Testing: Coin cells were cycled using a Scribner Associates Incorporated 580 Battery Test System between 1.8–2.6 V at a rate of C/10 based on the weight of sulfur. The cells were cycled to the desired depth of discharge (DoD) and then disassembled to extract cathodes for ex situ XTM experiments.

The capillary cell was cycled between 1.8–2.6 V at a rate of C/10 (I = 1.5931 µA) using a CompactStat potentiostat from Ivium Technologies. The applied current was based on the weight of sulfur in the cathode, estimated by a tomographic scan (tomogram) performed before the first discharge, with the cathode in its pristine state. Subsequently, tomograms were taken at different depths of discharge, indicated by the arrows in Figure 1.

Data Acquisition: XTM was performed at the TOMCAT Beamline (X02DA) at the Swiss Light Source, Paul Scherrer Institute, Switzerland.[52] Tomographic projections were acquired using a 21 keV monochromatic beam. A 20 µm thick LuAg:Ce scintillator was used to convert the X-ray beam to visible light which was subsequently magnified by a ULAPO20x objective. For the final image acquisition, a PCO.Edge camera (2560 × 2160 pixels) was employed giving a 0.325 µm voxel edge size, resulting in a total field-of-view of $0.8 \times 0.8 \times 0.7$ mm^3. For each tomogram, 1000 projections equally distributed over 180 degrees were acquired together with 10 dark and 100 flat images. For each projection, the exposure time was 50 ms, giving a total scanning time of approximately 1 min for a full tomogram. Figure 1 shows schematics of the capillary cell, and the region of interest (ROI) has been highlighted in Figure S1, Supporting Information. In the experiment the full cathode was in the field of view, whereas the Li metal anode was outside.

Data Reconstruction: Tomographic reconstructions were performed following the procedure by Marone et al.[53] For phase-contrast images, the phase information from the tomographic projections was obtained using a single defocused image method developed by Paganin et. al.,[49] using $\delta = 9.6\,10^{-7}$ and $\beta = 5.2\,10^{-9}$ and with a sample-to-detector distance of 0.02 m. All reconstructions were performed using the reconstruction tools available at the beamline.[53]

Coin Cell Image Processing: For visualization, absorption contrast tomograms were cropped and normalized to the intensity histogram of the tomogram corresponding to the pristine state. Representative ortho-slices were then extracted to illustrate the cathode microstructure at various depths of discharge.

Capillary Cell Image Processing: Absorption contrast tomograms were subject to a series of image pre-processing steps before segmentation in AVIZO. Tomograms were cropped to the volume interest for data reduction. Due to the absorption of the glass capillary and the liquid electrolyte, the volume of interest was corrected with a synthetic background image. The background image was created by making a median pixel intensity image from a stack of the first 500 slices of the tomogram, containing only capillary and electrolyte. Each slice was corrected by subtraction of the median background image. Subsequently, all tomograms were intensity histogram normalized to the first background-corrected tomogram and aligned to the first tomogram using pure rigid transformations.

Before segmentation in AVIZO, a non-local means filter (using AVIZO's default parameters) was used to decrease noise in all tomographic slices. Segmentation of sulfur particles was subsequently performed using thresholding, where the threshold value was chosen via visual inspection.

To verify the quality of the sulfur particle segmentation, contour plots of the binary segmented slices from each tomogram were overlaid on the corresponding raw reconstructed image for visual inspection. Verification images can be found in the Supporting materials. The registration and segmentation procedures were performed in AVIZO.

From the tomograms, elemental sulfur was segmented, and the mass of sulfur in the cathode at different states of discharge was determined from binary sulfur images multiplying the calculated S volume with the mass density (2.07 mg cm^{-3}).

Iso-surfaces of the segmented volumes were converted into stereolithography (STL) surface meshes and imported into ParaView to visualize 3D renderings of the evolution of sulfur particles in the entire cathode.

To follow the Li_2S precipitation, tomograms reconstructed using the Paganin method were used. The mean voxel intensity, computed on a region within the cathode structure, was used as an indication of the degree of Li_2S deposition onto the carbon-binder matrix.

Operando Optical Analysis: A Nikon D200 digital SLR camera with a 70–200 mm objective was used to collect optical images of the capillary cell automatically at 5 min intervals under ambient light. Color images were acquired at the highest sensor resolution (10MP). The camera was set to record 6 s of exposure, at ISO 100 and f-stop 32 (to ensure the capillary cell was completely inside the depth of field) with auto white balance. The capillary cell was placed against a defocused white background to ensure correct white balance.

All color images were processed using Mathematica's image processing functions. All images were spatially registered to the first image, to account for specimen stage movements during tomogram acquisitions. Subsequently, the color images were converted to grayscale (Figure S10, Supporting Information). The ROI was defined as a narrow region in the electrolyte spanning the distance between anode and cathode of the capillary cell. To quantify the intensity gradient, the ROI was divided into 19 equally spaced domains (see Figure S10, Supporting Information) and in each domain, the average greyscale value was determined as a function of time (depth of discharge). Further details can be found in the Supporting material.

Modeling of Polysulfide Diffusion: A 1D diffusion model, based on Fick's law, was used to model the data obtained from the optical image analysis. Simulations were run over 220 nodes (Figure S11, Supporting Information) with a time step of $\Delta t = 35$ ms and a spatial step of $\Delta x = 5.5 \times 10^{-2}$ mm giving a total length of 1.2 mm equal to the distance between the current collectors in the operando capillary cell. The central finite differences were used for the numerical solution of the differential equation. From n = 1 to 15 the nodes were considered to be part of the cathode, ≈0.1 mm in thickness. The node at n = 1 was the time-dependent source/sink of polysulfide, and the PS diffuse through the electrolyte confined in the cathode before reaching the bulk electrolyte volume between the two electrodes. The source of polysulfide was given by the mass change of sulfur (Figure S9, Supporting Information). More details on the model and its numerical implementation can be found in the Supporting Information.

Supporting Information

Supporting Information is available from the Wiley Online Library or from the author.

Acknowledgements

M.S. and S.A. contributed equally to this work. S.A. gratefully acknowledges financial support from the ESS & MAX IV: Cross

Border Science and Society project financed by the European Regional Development Fund. Travel support for the synchrotron experiment at the Swiss Light Source from DanScatt via the Danish Agency for Science, Technology, and Innovation was gratefully acknowledged by J.R.B., D.B., S.C.J., and R.E.J. A.M. and M.S. acknowledge support from FORMAS and Chalmers Areas of Advance Energy. The authors acknowledge the Paul Scherrer Institute, Villigen, Switzerland for provision of synchrotron radiation beamtime at the TOMCAT beamline X02DA of the SLS.

Conflict of Interest

The authors declare no conflict of interest.

Data Availability Statement

Contour plots of the binary segmented slices from each tomogram overlaid on the corresponding raw reconstructed image for visual inspection can be obtained free of charge from the Zenodo repository. https://zenodo.org/record/572377#.YGHVx2ixVB1.

Keywords

battery, Li—S, operando., tomography

Received: October 8, 2021
Revised: December 23, 2021
Published online: January 22, 2022

[1] X. Ji, K. T. Lee, L. F. Nazar, *Nat. Mater.* **2009**, *8*, 500.
[2] D. Larcher, J. M. Tarascon, *Nat. Chem.* **2015**,*7*, 19.
[3] A. Manthiram, Y. Fu, Y. S. Su, *Acc. Chem. Res.* **2013**, *46*, 1125.
[4] X. Ji, L. F. Nazar, *J. Mater. Chem.* **2010**, *20*, 9821.
[5] D. Zheng, X. Zhang, J. Wang, D. Qu, X. Yang, D. Qu, *J. Power Sources* **2016**, *301*, 312.
[6] M. Wild, L. O'Neill, T. Zhang, R. Purkayastha, G. Minton, M. Marinescu, G. J. Offer, *Energy Environ. Sci.* **2015**, *8*, 3477.
[7] S. Xiong, K. Xie, Y. Diao, X. Hong, *J. Power Sources* **2014**, *246*, 840.
[8] C. K. Chan, H. Peng, G. Liu, K. McIlwrath, X. F. Zhang, R. A. Huggins, Y. Cui, *Nat. Nanotechnol.* **2008**, *3*, 31.
[9] Z. L. Xu, J. Q. Huang, W. G. Chong, X. Qin, X. Wang, L. Zhou, J. K. Kim, *Adv. Energy Mater.* **2017**, *7*, 1602078.
[10] Z. L. Xu, J. K. Kim, K. Kang, *Nano Today* **2018**, *19*, 84.
[11] Y. Liu, Y. Pan, J. Ban, T. Li, X. Jiao, X. Hong, K. Xie, J. Song, A. Matic, S. Xiong, *Energy Storage Mater.* **2020**, *25*, 131.
[12] S. S. Zhang, *J. Power Sources* **2013**, *231*, 153.
[13] M. Agostini, J. Y. Hwang, H. M. Kim, P. Bruni, S. Brutti, F. Croce, A. Matic, Y. K. Sun, *Adv. Energy Mater.* **2018**, *8*, 1801560.
[14] S. Nanda, A. Bhargav, A. Manthiram, *Joule* **2020**, *4*, 1121.
[15] Z. L. Xu, S. J. Kim, D. Chang, K. Y. Park, K. S. Dae, K. P. Dao, J. M. Yuk, K. Kang, *Energy Environ. Sci.* **2019**, *12*, 3144.
[16] R. Kumar, J. Liu, J. Y. Hwang, Y. K. Sun, *J. Mater. Chem. A* **2018**, *6*, 11582.
[17] J. Hannauer, J. Scheers, J. Fullenwarth, B. Fraisse, L. Stievano, P. Johansson, *ChemPhysChem* **2015**, *16*, 2755.
[18] W. Zhu, A. Paolella, C. S. Kim, D. Liu, Z. Feng, C. Gagnon, J. Trottier, A. Vijh, A. Guerfi, A. Mauger, C. M. Julien, M. Armand, K. Zaghib, *Sustainable Energy Fuels* **2017**, *1*, 737.
[19] M. Hagen, P. Schiffels, M. Hammer, S. Dörfler, J. Tübke, M. J. Hoffmann, H. Althues, S. Kaskel, *J. Electrochem. Soc.* **2013**, *160*, A1205.
[20] H. L. Wu, L. A. Huff, A. A. Gewirth, *ACS Appl. Mater. Interfaces* **2015**, *7*, 1709.
[21] Q. Zou, Y. C. Lu, *J. Phys. Chem. Lett.* **2016**, *7*, 1518.
[22] M. U. M. Patel, R. Demir-Cakan, M. Morcrette, J. M. Tarascon, M. Gaberscek, R. Dominko, *ChemSusChem* **2013**, *6*, 1177.
[23] N. A. Cañas, D. N. Fronczek, N. Wagner, A. Latz, K. A. Friedrich, *J. Phys. Chem. C* **2014**, *118*, 12106.
[24] M. Cuisinier, P. E. Cabelguen, S. Evers, G. He, M. Kolbeck, A. Garsuch, T. Bolin, M. Balasubramanian, L. F. Nazar, *J. Phys. Chem. Lett.* **2013**, *4*, 3227.
[25] Y. Sun, Z. W. Seh, W. Li, H. Yao, G. Zheng, Y. Cui, *Nano Energy* **2015**, *11*, 579.
[26] J.-T. Yeon, J.-Y. Jang, J.-G. Han, J. Cho, K. T. Lee, N.-S. Choi, *J. Electrochem. Soc.* **2012**, *159*, A1308.
[27] S. Walus, C. Barchasz, J. F. Colin, J. F. Martin, E. Elkaïm, J. C. Leprêtre, F. Alloin, *Chem. Commun.* **2013**, *49*, 7899.
[28] J. Nelson, S. Misra, Y. Yang, A. Jackson, Y. Liu, H. Wang, H. Dai, J. C. Andrews, Y. Cui, M. F. Toney, *J. Am. Chem. Soc.* **2012**, *134*, 6337.
[29] J. H. Cheng, A. A. Assegie, C. J. Huang, M. H. Lin, A. M. Tripathi, C. C. Wang, M. T. Tang, Y. F. Song, W. N. Su, B. J. Hwang, *J. Phys. Chem. C* **2017**, *121*, 7761.
[30] C. Tan, T. M. M. Heenan, R. F. Ziesche, S. R. Daemi, J. Hack, M. Maier, S. Marathe, C. Rau, D. J. L. Brett, P. R. Shearing, *ACS Appl. Energy Mater.* **2018**, *1*, 5090.
[31] O. O. Taiwo, M. Loveridge, S. D. Beattie, D. P. Finegan, R. Bhagat, D. J. L. Brett, P. R. Shearing, *Electrochim. Acta* **2017**, *253*, 85.
[32] S. H. Yu, X. Huang, K. Schwarz, R. Huang, T. A. Arias, J. D. Brock, H. D. Abruña, *Energy Environ. Sci.* **2018**, *11*, 202.
[33] C. Tan, M. D. R. Kok, S. R. Daemi, D. J. L. Brett, P. R. Shearing, *Phys. Chem. Chem. Phys.* **2019**, *21*, 4145.
[34] F. Sun, K. Dong, M. Osenberg, A. Hilger, S. Risse, Y. Lu, P. H. Kamm, M. Klaus, H. Markötter, F. García-Moreno, T. Arlt, I. Manke, *J. Mater. Chem. A* **2018**, *6*, 22489.
[35] L. Zielke, C. Barchasz, S. Walu, F. Alloin, J. C. Leprêtre, A. Spettl, V. Schmidt, A. Hilger, I. Manke, J. Banhart, R. Zengerle, S. Thiele, *Sci. Rep.* **2015**, *5*, 10921.
[36] F. Sun, M. Osenberg, K. Dong, D. Zhou, A. Hilger, C. J. Jafta, S. Risse, Y. Lu, H. Markötter, I. Manke, *ACS Energy Lett.* **2018**, *3*, 356.
[37] A. Yermukhambetova, C. Tan, S. R. Daemi, Z. Bakenov, J. A. Darr, D. J. L. Brett, P. R. Shearing, *Sci. Rep.* **2016**, *6*, 35291.
[38] R. E. Johnsen, P. Norby, *J. Appl. Crystallogr.* **2013**, *46*, 1537.
[39] K. H. Wujcik, D. R. Wang, A. Raghunathan, M. Drake, T. A. Pascal, D. Prendergast, N. P. Balsara, *J. Phys. Chem. C* **2016**, *120*, 18403.
[40] U. Košir, I. Kralj Cigić, J. Markelj, S. Drvarič Talian, R. Dominko, *Electrochim. Acta* **2020**, *363*, 137227.
[41] H. Shin, M. Baek, A. Gupta, K. Char, A. Manthiram, J. W. Choi, *Adv. Energy Mater.* **2020**, *10*, 2001456.
[42] S. Drvarič Talian, G. Kapun, J. Moškon, A. Vizintin, A. Randon-Vitanova, R. Dominko, M. Gaberšček, *Chem. Mater.* **2019**, *31*, 9012.
[43] H. Schneider, T. Weiß, C. Scordilis-Kelley, J. Maeyer, K. Leitner, H. J. Peng, R. Schmidt, J. Tomforde, *Electrochim. Acta* **2017**, *243*, 26.
[44] A. Jozwiuk, B. B. Berkes, T. Weiß, H. Sommer, J. Janek, T. Brezesinski, *Energy Environ. Sci.* **2016**, *9*, 2603.
[45] N. Ding, L. Zhou, C. Zhou, D. Geng, J. Yang, S. W. Chien, Z. Liu, M. F. Ng, A. Yu, T. S. A. Hor, M. B. Sullivan, Y. Zong, *Sci. Rep.* **2016**, *6*, 33154.
[46] T. Danner, A. Latz, *Electrochim. Acta* **2019**, *322*, 134719.
[47] A. Vizintin, L. Chabanne, E. Tchernychova, I. Arčon, L. Stievano, G. Aquilanti, M. Antonietti, T. P. Fellinger, R. Dominko, *J. Power Sources* **2017**, *344*, 208.
[48] F. Y. Fan, W. C. Carter, Y. M. Chiang, *Adv. Mater.* **2015**, *27*, 5203.

[49] D. Paganin, S. C. Mayo, T. E. Gureyev, P. R. Miller, S. W. Wilkins, *J. Microsc.* **2002**, *206*, 33.
[50] C. Barchasz, F. Molton, C. Duboc, J. C. Leprêtre, S. Patoux, F. Alloin, *Anal. Chem.* **2012**, *84*, 3973.
[51] M. Safari, C. Y. Kwok, L. F. Nazar, *ACS Cent. Sci.* **2016**, *2*, 560.
[52] M. Stampanoni, A. Groso, A. Isenegger, G. Mikuljan, Q. Chen, A. Bertrand, S. Henein, R. Betemps, U. Frommherz, P. Böhler, D. Meister, M. Lange, R. Abela, *Dev. X-Ray Tomogr. V* **2006**, *6318*, 63180M.
[53] F. Marone, M. Stampanoni, *J. Synchrotron Radiat.* **2012**, *19*, 1029.